Computational Modeling of Cardiac Ablation Incorporating Electrothermomechanical Interactions

Singh, S. and Melnik, R.

ASME J of Medical Diagnostics. Nov 2020, 3(4): 041004 (12 pages)
Paper No: JESMDT-20-1033 https://doi.org/10.1115/1.4048536

The application of radio frequency ablation (RFA) has been widely explored in treating various types of cardiac arrhythmias. Computational modeling provides a safe and viable alternative to ex vivo and in vivo experimental studies for quantifying the effects of different variables efficiently and reliably, apart from providing a priori estimates of the ablation volume attained during cardiac ablation procedures. In this contribution, we report a fully coupled electrothermomechanical model for a more accurate prediction of the treatment outcomes during the radio frequency cardiac ablation. A numerical model comprising of cardiac tissue and the cardiac chamber has been developed in which an electrode has been inserted perpendicular to the cardiac tissue to simulate actual clinical procedures. Temperature-dependent heat capacity, electrical and thermal conductivities, and blood perfusion rate have been considered to model more realistic scenarios. The effects of blood flow and contact force of the electrode tip on the treatment outcomes of a fully coupled model of RFA have been systematically investigated. The numerical study demonstrates that the predicted ablation volume of RFA is significantly dependent on the blood flow rate in the cardiac chamber and also on the tissue deformation induced due to electrode insertion depth of 1.5 mm or higher.

==

The American Society of Mechanical Engineers

Journal of Engineering and Science in Medical Diagnostics and Therapy

ISSN: 2572-7958 | **eISSN:** 2572-7966

Computational Modeling of Cardiac Ablation Incorporating Electrothermomechanical Interactions

Sundeep Singh[1]
MS2Discovery Interdisciplinary Research Institute,
Wilfrid Laurier University,
75 University Avenue West,
Waterloo, ON N2 L 3C5, Canada
e-mail: ssingh@wlu.ca

Roderick Melnik
MS2Discovery Interdisciplinary Research Institute,
Wilfrid Laurier University,
75 University Avenue West,
Waterloo, ON N2 L 3C5, Canada;
Basque Center for Applied Mathematics (BCAM),
Alameda de Mazarredo 14,
Bilbao E-48009, Spain
e-mail: rmelnik@wlu.ca

The application of radio frequency ablation (RFA) has been widely explored in treating various types of cardiac arrhythmias. Computational modeling provides a safe and viable alternative to ex vivo and in vivo experimental studies for quantifying the effects of different variables efficiently and reliably, apart from providing a priori estimates of the ablation volume attained during cardiac ablation procedures. In this contribution, we report a fully coupled electrothermomechanical model for a more accurate prediction of the treatment outcomes during the radio frequency cardiac ablation. A numerical model comprising of cardiac tissue and the cardiac chamber has been developed in which an electrode has been inserted perpendicular to the cardiac tissue to simulate actual clinical procedures. Temperature-dependent heat capacity, electrical and thermal conductivities, and blood perfusion rate have been considered to model more realistic scenarios. The effects of blood flow and contact force of the electrode tip on the treatment outcomes of a fully coupled model of RFA have been systematically investigated. The numerical study demonstrates that the predicted ablation volume of RFA is significantly dependent on the blood flow rate in the cardiac chamber and also on the tissue deformation induced due to electrode insertion depth of 1.5 mm or higher. [DOI: 10.1115/1.4048536]

Introduction

Radio frequency ablation (RFA) is one of the most promising minimally invasive treatment modalities that has been widely and effectively used for treating different types of soft tissue tumors in clinical practices [1–4]. RFA has also been explored in the treatment of certain types of cardiac arrhythmias, including atrial fibrillation. In the past two decades, radio frequency (RF) assisted cardiac ablation has become one of the most useful and widely used first-line treatment options in the field of cardiac electrophysiology due to its high efficacy and safety profile [5]. During RFA of the cardiac tissue, a catheter is navigated into the heart to locally heat and destroy small tissue region, so as to electrically isolate the arrhythmogenic tissues that generate or propagate arrhythmia [5,6]. RF current is delivered into the myocardium tissue utilizing the catheter that induces thermal lesion formation through resistive heating of myocardial tissue and leads to irreversible damage at a temperature of 50 °C, or higher. The overall goal of the RFA is to provide optimal heat transfer within the target tissue that can result in the attainment of the enhanced ablation zone and minimize the effect of factors that hinders the efficient heat delivery to the tissue.

Numerical modeling and simulations play a vital role in the design and development of new systems and protocols for RFA, along with the improvement and optimization of the existing protocols. Numerical simulations could serve as a powerful predictive tool for providing a reasonable estimate of the treatment outcomes to the clinical practitioners, rapidly and at a low cost. They also assist in our better understanding of the effects of different extrinsic and intrinsic factors on the efficacy of RFA [7–13]. Several computational studies have been reported in the literature on the modeling of cardiac ablation utilizing coupled thermo-electric framework [14–17]. Further, most of these modeling studies on cardiac ablation have clearly neglected the influence of tissue deformation under the application of force exerted due to the insertion of the catheter. More recently, the mechanical model has been incorporated in Refs. [18] and [19] for modeling the tissue deformation under the application of force exerted due to the insertion of the electrode. However, very limited work has been reported in the literature that takes into account the thermoelastic deformations induced due to the nonuniform temperature distribution within the cardiac tissue during RFA. Importantly, the attainment of higher temperatures within the biological tissues during RFA could significantly contribute to variations in their shape or size due to the induced thermal strain. Thus, in a quest for minimizing the deviations between the numerically predicted and experimentally obtained lesion volumes and more accurately quantifying the treatment outcomes of the cardiac ablation, we report a fully coupled electrothermomechanical model that accounts for the tissue deformation induced due to electrode insertion as well as due to thermal stresses [7]. We systematically investigated the effect of contact force exerted on the cardiac tissue from the electrode and the blood flow rates on the treatment outcomes of cardiac ablation.

Problem Formulation and Mathematical Modeling

Figure 1 presents the two-dimensional axisymmetric computational domain considered in this study for simulating the cardiac ablation procedure, which comprises a fragment of cardiac tissue, electrode, and blood chamber [16]. An open-irrigated electrode (7 Fr diameter and 4 mm length) has been considered that is placed perpendicular to the cardiac tissue and is surrounded by the circulating blood (cardiac chamber) [16,17]. A contact force is applied at the electrode tip of the catheter (i.e., insulated part of the electrode) that results in the mechanical deformation of the tissue surface along with the electrode insertion. Motivated by Refs. [17–19], four different values of insertion depth of the electrode have been considered in this study, viz., 0.5, 1, 1.5, and 2 mm.

[1]Corresponding author.

Contributed by the Applied Mechanics Division Technical Committee on Dynamics & Control of Structures & Systems (AMD-DCSS) of ASME for publication in the Journal of Engineering and Science in Medical Diagnostics and Therapy. Manuscript received July 17, 2020; final manuscript received September 21, 2020; published online October 13, 2020. Assoc. Editor: Ramjee Repaka.

Notably, considered values of the insertion depth of the electrode lie within the range of contact force between 10 and 40 g that has proved to be safer and effective in clinical trials reported in the literature [19]. The electrothermomechanical properties of different materials considered in the present computational study have been summarized in Table 1 [7,16–19].

The thermal problem of cardiac ablation is solved utilizing the generalized Fourier conduction based Pennes bioheat transfer equation modified by the enthalpy method that incorporates the liquid–vapor phase change to model tissue vaporization within the biological tissue [3,7,17], and is given by

$$\frac{\partial(\rho h)}{\partial t} = k\nabla^2 T - \rho_b c_b \omega_b (T - T_b) + Q_m + Q_p \tag{1}$$

where ρ is the density (kg/m^3), h is the enthalpy (J/m^3), ρ_b is the density of blood (kg/m^3), c_b is the specific heat capacity of the blood (J/(kg·K)), k is the thermal conductivity (W/(m·K)), ω_b is the blood perfusion rate (1/s), T_b is the blood temperature (= 37 °C), and T is the unknown temperature (K) to be computed within the cardiac tissue. The term $\rho_b c_b \omega_b (T - T_b)$ accounts for the microvascular heat sink effect, Q_p is the radio frequency heat source (W/m^3), and Q_m is the metabolic heat generation (W/m^3) that has been neglected due to its insignificant contribution in comparison to the other terms [14–19]. Further, the enthalpy of the biological tissue is related to the temperature by

$$\frac{\partial(\rho h)}{\partial t} = \frac{\partial T}{\partial t} \cdot \begin{Bmatrix} \rho_l c_l & 0 \le T \le 99\,^\circ\text{C} \\ H_{fg} C & 99\,^\circ\text{C} < T \le 100\,^\circ\text{C} \\ \rho_g c_g & T > 100\,^\circ\text{C} \end{Bmatrix} \tag{2}$$

where ρ_i and c_i are the density and specific heat of tissue before phase-change (subscript $i = l$ refers to liquid tissue phase at temperatures below 100 °C and subscript $i = g$ refers to postphase-change above 100 °C), H_{fg} is the latent heat (= 2.162×10^9 J/m^3), i.e., the product of water latent heat of vaporization and water density at 100 °C, and C is the tissue water content inside the tissue (=75%).

Moreover, at the frequency range used during cardiac ablation (≈500 kHz), the wavelength of the electromagnetic field is several orders of magnitude larger than the size of the active electrode, and thus, the biological tissue can be considered totally resistive and a simplified version of Maxwell's equations (known as a quasi-static approximation) can be used to solve the electromagnetic problem without compromising accuracy [3,4]. The volumetric heat generation (Q_p) by electromagnetic field within the biological tissue is given by

$$Q_p = \sigma |E|^2 \tag{3}$$

where σ is the temperature-dependent electrical conductivity (S/m) and the electric field intensity (E) for the quasi-static approximation of Maxwell's equations is computed from the gradient of voltage (V), as

$$E = -\nabla V \tag{4}$$

which in the absence of internal electric sources satisfies the generalized Laplace equation

$$\nabla \cdot \sigma \nabla V = 0 \tag{5}$$

Further, the electrical conductivity, thermal conductivity, and blood perfusion rate of the cardiac tissue have been modeled as a temperature-dependent function [3,17] and are given by Eqs. (6)–(8), respectively, as

$$\sigma(T) = \begin{Bmatrix} \sigma_0 \exp^{0.015(T - T_b)} & \text{for } T \le 99\,^\circ\text{C} \\ 2.5345\sigma_0 & \text{for } 99\,^\circ\text{C} < T \le 100\,^\circ\text{C} \\ 2.5345\sigma_0[1 - \Delta\sigma_0(T - 100\,^\circ\text{C})] & \text{for } 100\,^\circ\text{C} < T \le 105\,^\circ\text{C} \\ 0.025345\sigma_0 & \text{for } T > 105\,^\circ\text{C} \end{Bmatrix} \tag{6}$$

$$k(T) = \begin{Bmatrix} k_0 + \Delta k(T - T_b) & \text{for } T \le 100\,^\circ\text{C} \\ k_0 + \Delta k(100\,^\circ\text{C} - T_b) & \text{for } T > 100\,^\circ\text{C} \end{Bmatrix} \tag{7}$$

$$\omega_b(T) = \begin{Bmatrix} \omega_{b,0} & \text{for } T < 50\,^\circ\text{C} \\ 0 & \text{for } T \ge 50\,^\circ\text{C} \end{Bmatrix} \tag{8}$$

where σ_0, k_0, and $\omega_{b,0}$ are the electrical conductivity, thermal conductivity, and blood perfusion rate, respectively, of the myocardium tissue at baseline temperature of T_b (=37 °C) as presented in Table 1, $\Delta\sigma_0$ (=19.8%) is the decline of myocardial electrical conductivity per °C increase in the temperature beyond 100 °C due to tissue charring and water vaporization, Δk_0 (=0.12%) is the increase of myocardial thermal conductivity per °C increase in the temperature, and T is the temperature computed from the modified Pennes bioheat transfer equation Eq. (1).

Motivated by Refs. [16] and [17], the ablation (or damage) volume induced during the cardiac ablation ($\dot{V}$) has been quantified using the 50 °C isotherm contour (i.e., the volume of cardiac tissue having a temperature ≥ 50 °C post-RFA procedure), which corresponds to a reasonable estimate of the irreversible myocardial injury during hyperthermic ablation, and is given by [20,21]

$$\dot{V} = \iiint_{\Omega} dV\,(\text{mm}^3) \quad (\text{where } \Omega \ge 50\,^\circ\text{C}) \tag{9}$$

The general form of the thermo-elastic wave equation for the nonrigid mechanics is given by [3,7]

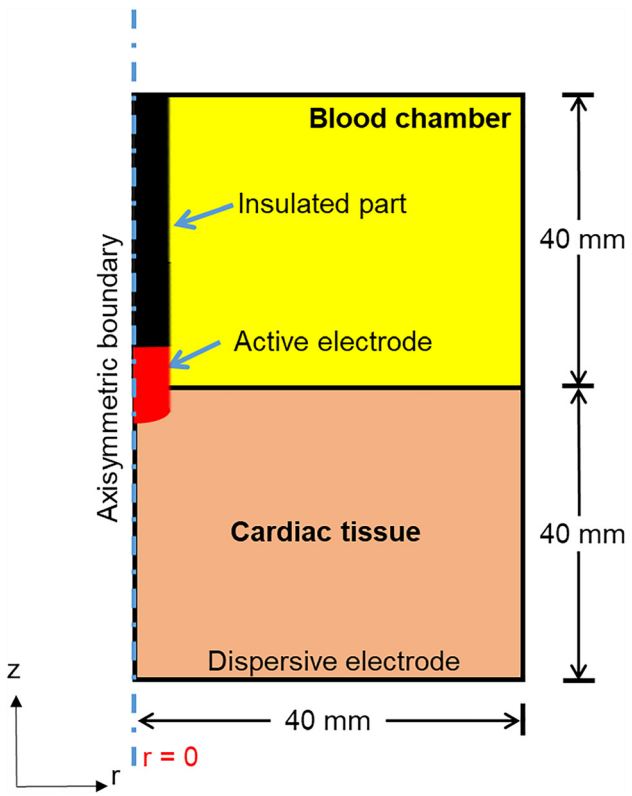

Fig. 1 Schematic of a two-dimensional axisymmetric model of the cardiac ablation considered in this study (not to scale)

Table 1 Electrothermomechanical properties of different materials considered in this study

	Myocardium/cardiac tissue				
Parameter	Liquid phase	Gas phase	Blood/cardiac chamber	Electrode (active part)	Catheter (insulated part)
ρ (kg/m^3)	1060	370.44	1000	21,500	70
c (J/(kg·K))	3111	2155.92	4180	132	1045
k (W/(m·K))	$k_0 = 0.54$		0.54	71	0.026
ω_b (s^{-1})	$\omega_{b,0} = 0.017$		—	—	—
σ (S/m)	$\sigma_0 = 0.6$		0.99	4.6×10^6	10^{-5}
α (K^{-1})	1×10^{-4}		—	—	—

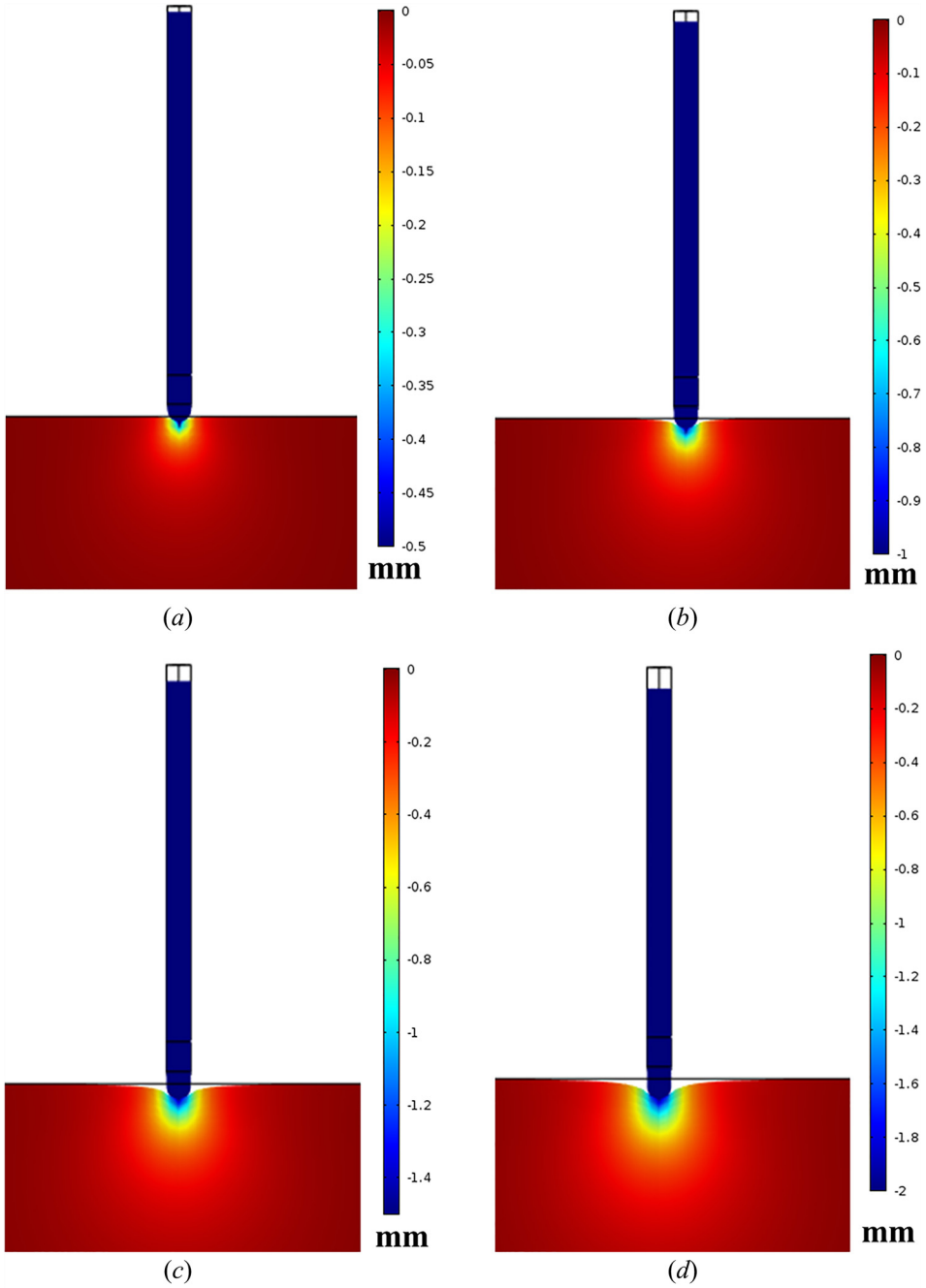

Fig. 2 Displacement field distributions and deformation at the electrode-tissue interface for electrode insertion depth of: (*a*) 0.5 mm, (*b*) 1 mm, (*c*) 1.5 mm, and (*d*) 2 mm

$$\rho \frac{\partial^2 u}{\partial t^2} = \bar{\sigma}_{ij,j} + \bar{F} \tag{10}$$

where ρ is the density of the material, $\bar{\sigma}$ is the stress tensor ($i,j = 1,2,3$ are the tensor indices representing geometry's coordinate axes), u is the mechanical displacement vector, t is the time, and $\bar{F}$ is the external body force. In this study, the RF electrode has been modeled as linearly elastic, isotropic, and homogeneous material having Young's modulus of elasticity as 168 GPa and Poisson's ratio as 0.38 [19]. The stress–strain relationship for the linearly elastic material is given by [3,7]

$$\bar{\sigma}_{ij} = 2\mu\varepsilon_{ij} + \lambda\varepsilon_{kk}\delta_{ij} \tag{11}$$

where $\varepsilon = \left[(\nabla u^T + \nabla u)/2\right]$ is the strain tensor (subscript $i,j = 1, 2, 3$ are the tensor indices representing geometry's coordinate axes and subindices $_{kk}$ indicate the trace of the strain tensor), $\mu = \left[\bar{E}/(2(1+\nu))\right]$ and $\lambda = \left[\nu\bar{E}/((1+\nu)(1-2\nu))\right]$ are the Lame's constants, $\bar{E}$ is the Young's modulus of elasticity, and ν is the Poisson's ratio and δ is the Kronecker delta function given by [3,7]

$$\delta_{ij} = \begin{cases} 1 & \text{for } i = j \\ 0 & \text{for } i \neq j \end{cases} \tag{12}$$

The myocardium tissue has been modeled as a nearly incompressible, isotropic, and homogenous hyperelastic material. The Cauchy-stress tensor for the hyperelastic material can be expressed as [22,23]

$$\bar{\sigma} = J^{-1}\frac{\partial W(F)}{\partial F}F^T \tag{13}$$

where F is the deformation gradient and J is the volume ratio (=det(F)) and W is a function of the Green strain components. In this study, the Mooney–Rivlin model has been used for describing the strain energy function of the hyperelastic myocardium tissue [19]

$$W = C_1(I_1 - 3) + C_2(I_2 - 3) + D_1[\exp(D_2(I_1 - 3)) - 1] \tag{14}$$

where I_1 and I_2 are the first and second strain invariants, respectively, C_1 (=351 Pa), C_2 (=0), D_1 (=63.3 Pa), and D_2 (=5.3) are the material parameters adopted from Ref. [19]. Further, the thermal expansion of the hyperelastic myocardial tissue is modeled as [23]

$$J^{\text{th}} = (1 + \varepsilon^{\text{th}})^3$$
$$\varepsilon^{\text{th}} = \int_{T_b}^{T} \alpha dT \tag{15}$$

where J^{th} is the thermal volume ratio, ε^{th} is the linear thermal expansion strain, and α is the thermal expansion coefficient.

A constant voltage cardiac ablation has been modeled by applying the Dirichlet voltage boundary condition at the active electrode surface whereby a fixed constant voltage of 25 V has been applied for 60 s [14]. The dispersive (ground) electrode has been modeled by applying a 0 V at the bottom surface of the computational domain, so as to mimic the RF current flow between the active and ground electrodes in a monopolar configuration. All the other outer surfaces of the model have been subjected to the Neumann electrical boundary condition of null electric flux. The initial voltage of the entire computational domain has been considered to be 0 V. The effect of the saline flow from the holes of an open-irrigated electrode has been modeled by specifying a constant temperature of 45 °C at the cylindrical zone of the electrode tip, leaving the semispherical part inserted within the tissue free, as in previous numerical studies [16,17]. Notably, this approximation for modeling an open-irrigated electrode has earlier proved to be suitable for predicting the ablation depth and maximum temperature reached within the tissue during cardiac ablation for all time steps [16].

Further, the effect of blood flow inside the cardiac chamber has been modeled by specifying the thermal convective coefficients at the electrode–blood (h_E) and the tissue–blood (h_T) interfaces to reduce computational complexity. Although this modeling approach of blood flow within the cardiac chamber does not provide a realistic blood temperature distribution during cardiac ablation, it does predict the ablation depth reasonably well [16,17]. In this study, we considered two values of blood velocity, viz., 8.5×10^{-3} m/s and 3×10^{-3} m/s representing the high and low blood flow rates within the cardiac chamber, respectively. For these values of the blood flow rates, the respective values of convective heat transfer coefficients are: $h_E = 3346$ and 2059 W/m^2·K; and $h_T = 610$ and 265 W/m^2·K corresponding to the high and low blood flow rates, respectively [14,17]. A constant temperature (= 37 °C) thermal boundary condition has been specified at all the outer boundaries of the computational domain that is also the initial model temperature, except at the electrode tip which was considered to be 22 °C, so as to take into account the saline inflow from the open-irrigated electrode [17].

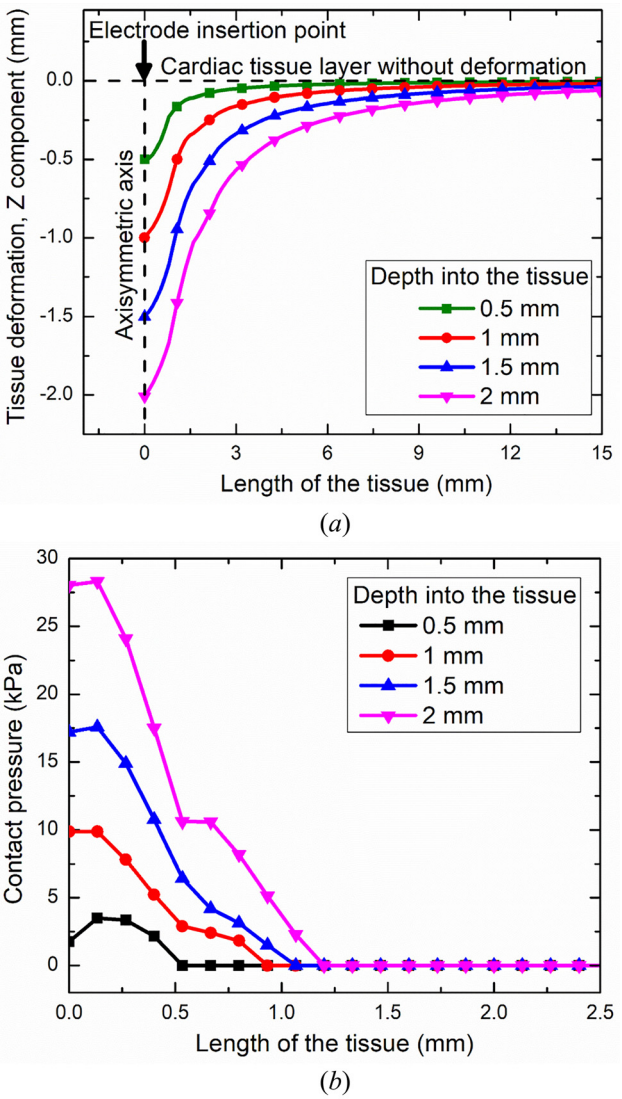

Fig. 3 (*a*) Tissue deformation and (*b*) contact pressure distribution at the electrode-tissue interface for the electrode insertion depth of: (*a*) 0.5 mm, (*b*) 1 mm, (*c*) 1.5 mm, and (*d*) 2 mm

Regarding the mechanical boundary conditions, a prescribed displacement in the vertically downward direction (i.e., *z-axis*) has been applied to the RF electrode (viz., 0.5, 1, 1.5, and 2 mm) to simulate the effect of contact force on the cardiac ablation [17–19]. The prescribed displacement at the electrode surface in the radial direction has been considered to be zero and the fixed constraint on the displacement has been applied at the bottom surface of the computational domain [19]. The initial stress and strain have been set to zero for the entire model. Moreover, the electrical, thermal, and mechanical continuity boundary conditions have been imposed at each interface of the computational domain.

A finite element method (FEM) based COMSOL MULTIPHYSICS 5.5 software [24] has been used to solve the coupled electrothermomechanical problem using quadratic (second-order) shape functions. A sigmoid function has been used to handle the abrupt changes in myocardium tissue properties at phase change temperature of 100 °C. It is noteworthy to mention that the computational model of cardiac ablation has been solved in two steps. The first step computes the tissue deformation induced due to the contact force exerted by the RF electrode on the cardiac tissue for different insertion depth of the electrode (= 0.5, 1, 1.5, and 2 mm) considering only the mechanical model, whereby the cardiac tissue is modeled as a hyperelastic material and RF electrode is modeled as a linearly elastic material. In the next step based on the computed deformation of the tissues for different insertion depth of the electrode, a fully coupled electrothermomechanical model has been solved to compute the electric field distributions, temperature distributions, ablation volumes and thermally induced stresses within the cardiac tissue during the RFA procedure. Further, the computational domain has been discretized using the spatial heterogeneous triangular mesh elements with around 12,000 elements having a minimum element size of 1.57 μm and a maximum element size of 0.785 mm. While modeling the first step, where the deformation induced within the cardiac tissue due to the electrode insertion has to be computed, the destination boundary (i.e., cardiac tissue) has a finer mesh size compared to the source boundary (i.e., RF electrode). For the second step, where a fully coupled electrothermomechanical model has been solved, an extra mesh refinement has been applied at the electrode-tissue interface where the highest thermal, mechanical and electrical gradients were expected. The final mesh size has been obtained after conducting the mesh convergence tests by progressively refining the mesh until the absolute error for maximum temperature and von Mises stress is less than 0.5% compared to the previous mesh size and accordingly the previous mesh size was considered as the final optimal mesh size for conducting FEM simulations. All simulations have been conducted on a 64-bit 10 core Intel Xeon E5-2680 v22.80 GHz processor (Santa Clara, CA) with a solution time of less than 30 min.

Results and Discussion

The effect of the insertion depth of the RF electrode on the deformation of cardiac tissue during the RFA procedure has been presented in Fig. 2. As mentioned earlier, we have considered four values of the insertion depth, viz., 0.5, 1, 1.5, and 2 mm, in our analysis, so as to mimic the most reliable and frequently utilized range of the penetration depth in clinical trials. As evident from Fig. 2, the deformation of the cardiac tissue at the electrode-tissue interface increases with an increase in the insertion depth of the electrode. The corresponding displacement field distributions

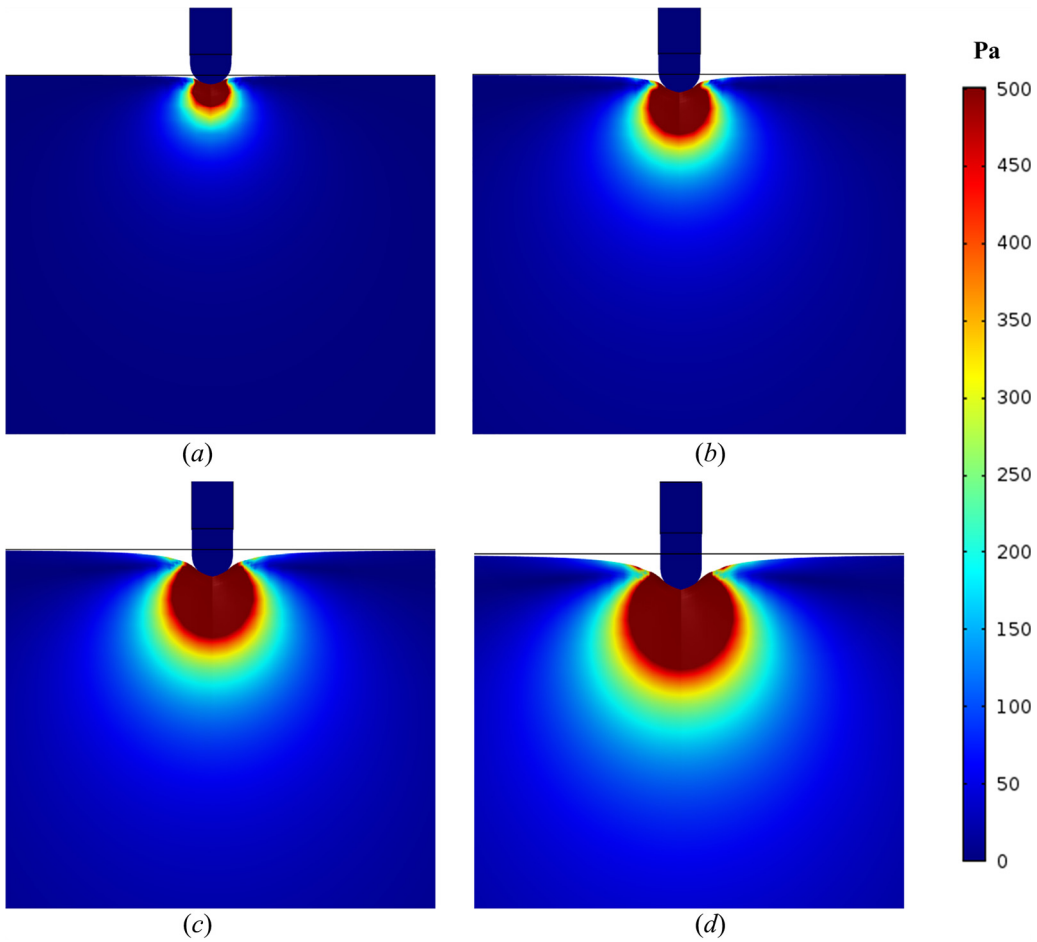

Fig. 4 Von Mises stress distributions within the cardiac tissue for the electrode insertion depth of: (*a*) 0.5 mm, (*b*) 1 mm, (*c*) 1.5 mm, and (*d*) 2 mm

have also been presented in Fig. 2 for different insertion depth of the electrode considered in the present analysis. Further, the comparative analysis of the induced deformation of the cardiac tissue due to RF electrode insertion for different depths has been presented in Fig. 3(*a*). As evident from Fig. 3(*a*), the deformation of the cardiac tissue at the electrode-tissue interface is quite predominant for all cases. Moreover, the contact pressure exerted by the electrode on the cardiac tissue has been presented in Fig. 3(*b*). It can be seen from Fig. 3(*b*) that the contact pressure increases with the increase in the insertion depth of the electrode and the maximum effect is mainly confined to the radius of the electrode, i.e., up to 1.16 mm or so. Figure 4 presents the von Mises stress distribution corresponding to different values of the insertion depth of the RF electrode. The maximum value of von Mises stress induced within the cardiac tissue for the electrode insertion depth of 0.5, 1, 1.5, and 2 mm have been found to be 1.61 kPa, 4.50 kPa, 8.03 kPa, and 38.8 kPa, respectively. Further, as evident from Fig. 4, the increase in contact force at the electrode results in a significant increase in the induced von Mises stress, which is evident from its wider and deeper reach within the cardiac tissue.

The temperature distributions obtained from the fully coupled electrothermomechanical model of cardiac ablation have been

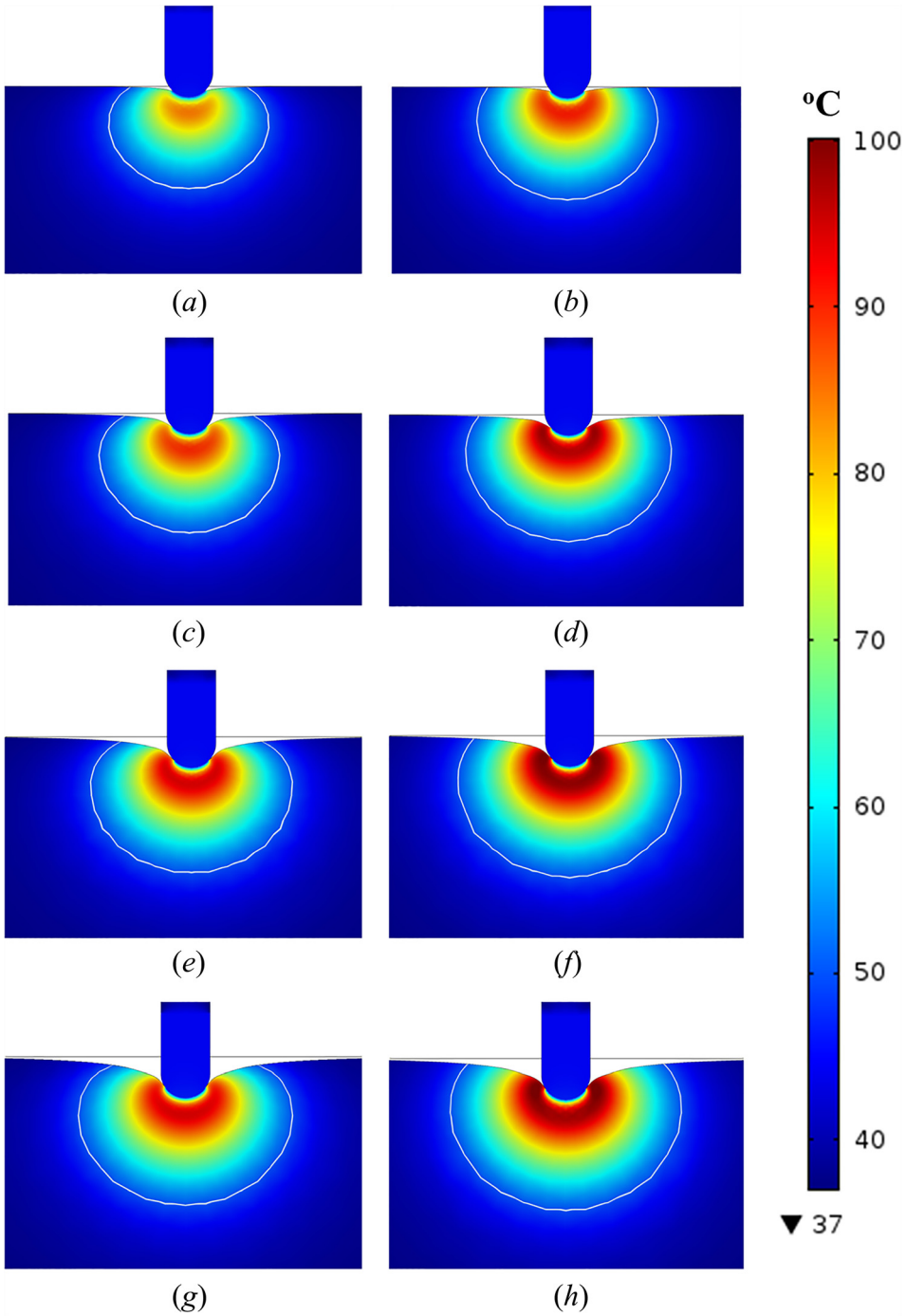

Fig. 5 Temperature distributions obtained in the cardiac tissue after 60 s of RFA under the electrode insertion depth of: (*a*) and (*b*) 0.5 mm, (*c*) and (*d*) 1 mm, (*e*) and (*f*) 1.5 mm, and (*g*) and (*h*) 2 mm. (*a*), (*c*), (*e*), and (*g*) are for high blood flow while (*b*), (*d*), (*f*), and (*h*) are under low blood flow conditions (solid white lines denotes the lesion boundaries corresponding to 50 °C isotherm).

presented in Fig. 5 for different values of insertion depth of the electrode, viz., Figs. 5(*a*) and 5(*b*) for 0.5 mm, Figs. 5(*c*) and 5(*d*) for 1 mm, Figs. 5(*e*) and 5(*f*) for 1.5 mm, and Figs. 5(*g*) and 5(*h*) for 2 mm. The left side of Fig. 5 (i.e., Figs. 5(*a*), 5(*c*), 5(*e*), and 5(*g*) denotes the temperature distribution obtained under the condition of high blood flow rate within the cardiac chamber surrounding the open-irrigated electrode, while the right side (i.e., Figs. 5(*b*), 5(*d*), 5(*f*), and 5(*h*)) denotes the temperature distribution obtained with low blood flow rate condition. It can be seen from Fig. 5 that the blood flow rate within the cardiac chamber significantly affects the temperature distribution obtained within the cardiac tissue during the RFA procedure, and this is true for all values of the RF electrode insertion depths. The maximum values of the temperature within the tissue after 60 s of cardiac ablation for high blood flow conditions have been found to be 84.7 °C, 89.8 °C, 94.3 °C, and 94.4 °C for the electrode insertion depth of 0.5, 1, 1.5, and 2 mm, respectively. While for the low blood flow rate conditions within the cardiac chamber, the maximum values of temperature have been found to be 90.8 °C, 98.1 °C, 101.23 °C, and 101.33 °C for the electrode insertion depth of 0.5, 1, 1.5, and 2 mm, respectively.

The temporal variation of the ablation volume for different values of the insertion depth of the electrode during the cardiac ablation has been presented in Fig. 6. As evident from Fig. 6, the predicted ablation volume for low blood flow conditions is always higher as compared to the high blood flow condition during the whole ablation time. Moreover, the deviation between the ablation volumes obtained with the high and low blood flow conditions is quite negligible initially up to the first 10 s and increases thereafter. The maximum deviation between the ablation volume obtained with the high and low blood flow conditions has been found for the insertion depth of 0.5 mm. In comparison to the low blood flow, the predicted ablation volumes after 60 s of cardiac ablation with high blood flow decrease by 26.38%, 25.67%, 20.23%, and 18.21% for the electrode insertion depth of 0.5, 1, 1.5, and 2 mm, respectively. Further, the predicted ablation volumes at the end of 60 s of cardiac ablation procedure increase by 44.76%, 96.72%, and 117.61% for the electrode insertion depth of 1, 1.5, and 2 mm, respectively, in comparison to the ablation volume predicted with the electrode insertion depth of 0.5 mm for high blood flow condition. For the low blood flow condition, the

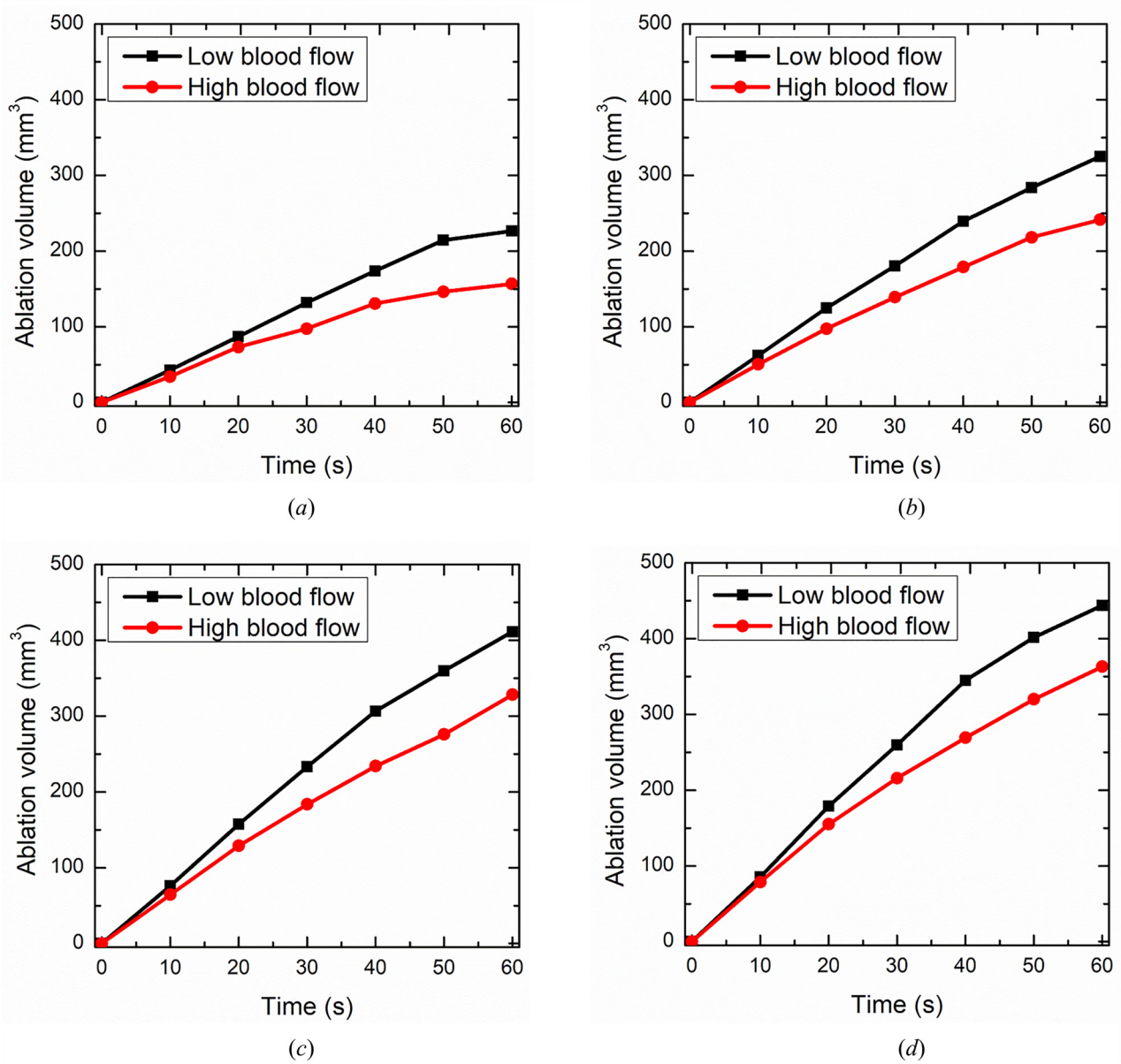

Fig. 6 Temporal variation of the ablation volume attained after 60 s of cardiac ablation under the electrode insertion depth of: (*a*) 0.5 mm, (*b*) 1 mm, (*c*) 1.5 mm, and (*d*) 2 mm

respective increase in the ablation volumes have been found to be 43.37%, 81.55%, and 95.87% for the electrode insertion depth of 1, 1.5, and 2 mm, respectively, when compared to the ablation volume predicted with 0.5 mm electrode insertion depth. This abrupt rise in the predicted ablation volume with the increase of insertion depth of the electrode can be attributed to the fact that the electrode-tissue contact volume increases as the insertion depth or the contact force increases, resulting in improved RF energy delivery to the tissue and thereby enhancing the ablation volume and thus overall effectiveness of the cardiac ablation. Conversely, for the low contact force, the majority of the RF energy will be taken away by the blood flow within the cardiac chamber owing

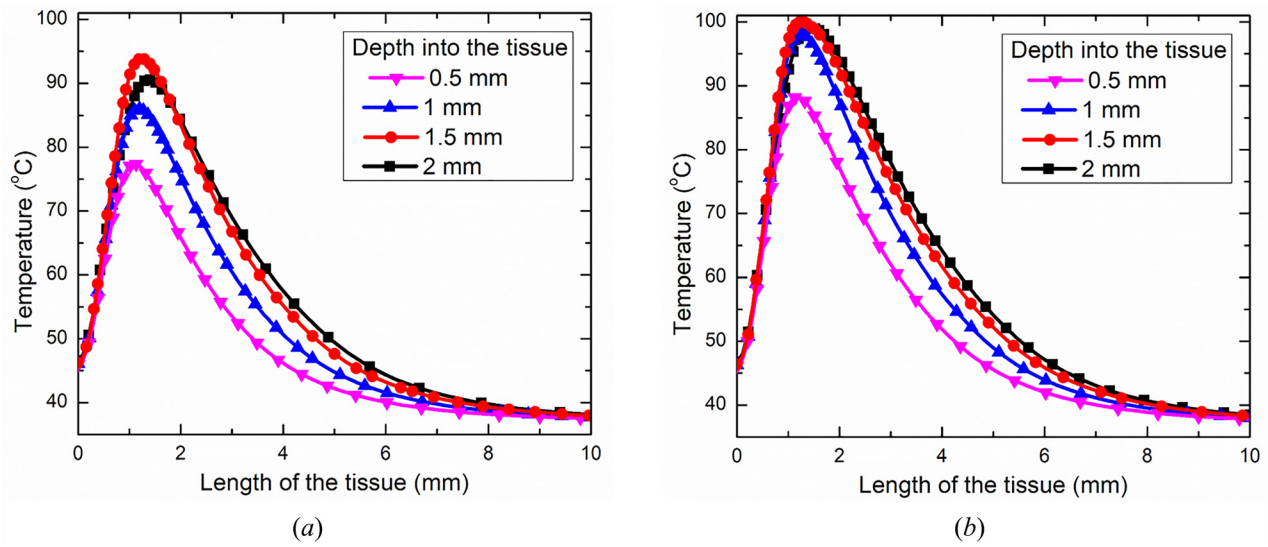

Fig. 7 Temperature distributions obtained after 60 s of cardiac ablation as a function of distance from the electrode tip (measured perpendicular to the electrode surface) under different electrode insertion depth for: (*a*) high blood flow and (*b*) low blood flow conditions

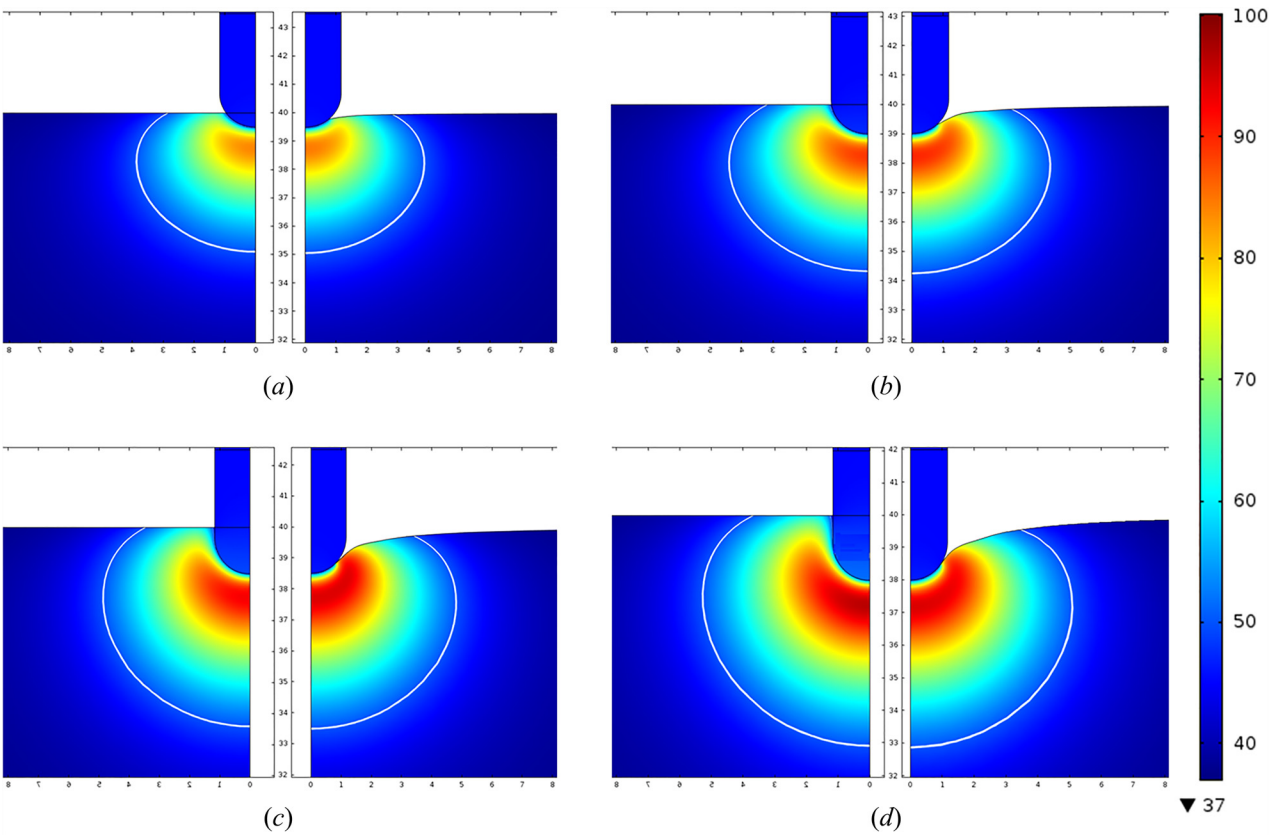

Fig. 8 Temperature distributions (in °C) obtained after 60 s of cardiac ablation under high blood flow conditions for the electrode insertion depth of: (*a*) 0.5 mm, (*b*) 1 mm, (*c*) 1.5 mm, and (*d*) 2 mm. Left column is for the case where the tissue deformation has been neglected while right column is for the case where the tissue deformation has been considered (the axes are represented in mm, and solid white lines denote the lesion boundaries corresponding to 50 °C isotherm).

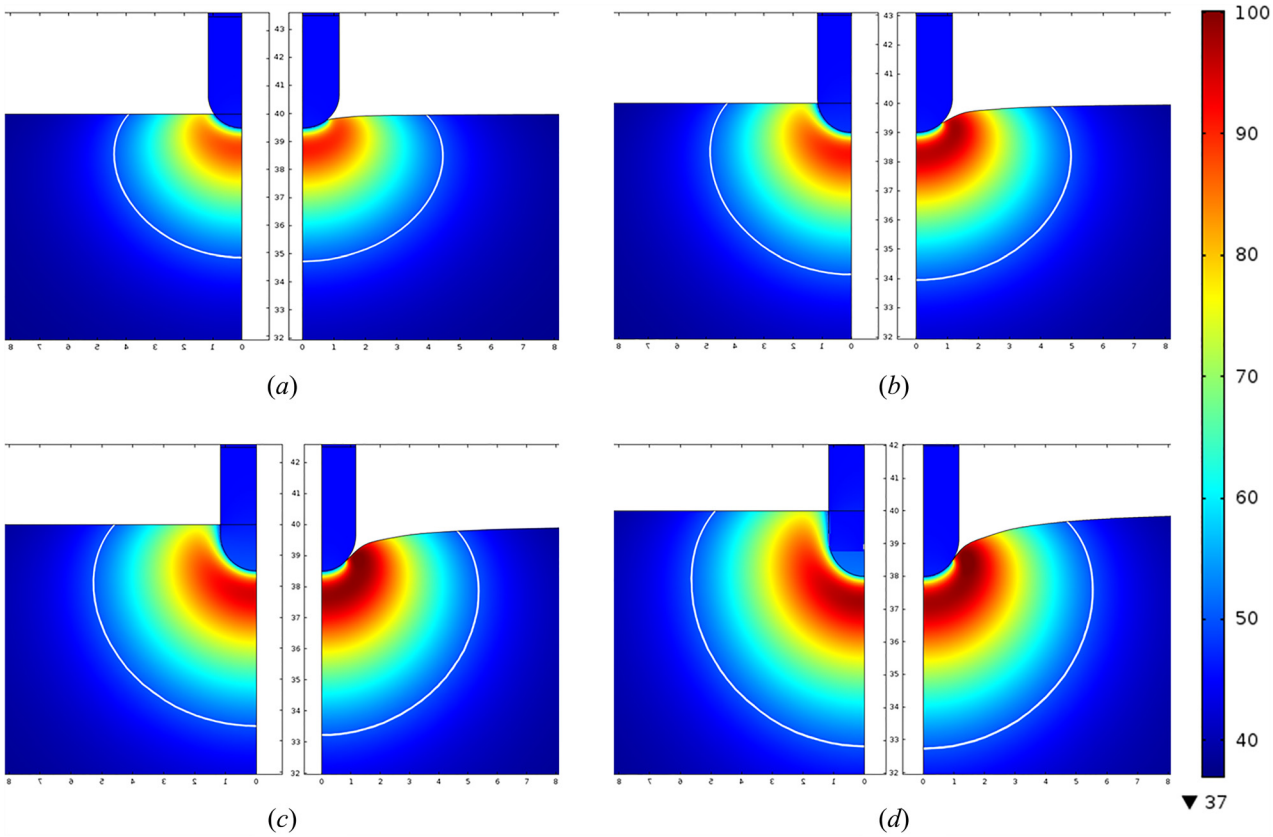

Fig. 9 Temperature distributions (in ° C) obtained after 60 s of cardiac ablation under low blood flow conditions for the electrode insertion depth of: (*a*) 0.5 mm, (*b*) 1 mm, (*c*) 1.5 mm, and (*d*) 2 mm. Left column is for the case where the tissue deformation has been neglected while right column is for the case where the tissue deformation has been considered (the axes are represented in mm, and solid white lines denote the lesion boundaries corresponding to 50 °C isotherm).

to insufficient electrode-tissue contact, and thus reducing the adequate delivery of the energy to the target tissue that further results in a decline in the obtained ablation volume. The temperature distributions across a line perpendicular to the electrode tip under different electrode insertion depths have been presented in Fig. 7 for high and low blood flow conditions. As evident from Fig. 7, the temperature at the proximity of the electrode is lower due to the cooling effect induced due to the saline irrigation that

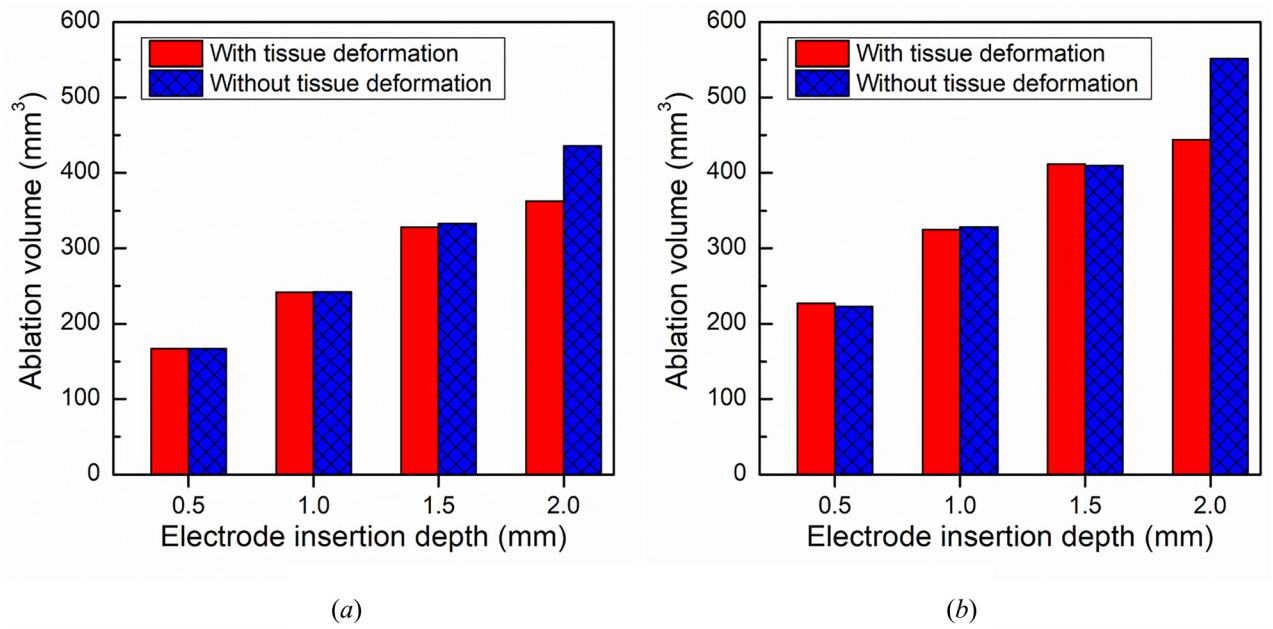

Fig. 10 Comparison of the ablation volume attained after 60 s of cardiac ablation for different values of insertion depth of the electrode with and without consideration of tissue deformation at the electrode-tissue interface for: (*a*) high blood flow and (*b*) low blood flow conditions

shifts the peak temperature a few mm away from the tip of the electrode. Further, the temperature distribution obtained for lower blood flow condition is on the higher side when compared to higher blood flow condition, and the length of tissue exposed to the temperature of 50 °C or higher increases with the increase in the insertion depth of the electrode.

The comparative analysis of the temperature distribution predicted with and without consideration of tissue deformation during cardiac ablation has been presented in Figs. 8 and 9, for high and low blood flow rates, respectively. Importantly, the left side of each subfigures of Figs. 8 and 9 denotes the temperature distribution predicted without considering tissue deformation (i.e., assuming sharp insertion of the electrode) while the right side denotes the temperature distribution predicted with consideration of tissue deformation induced at the tissue-electrode contact surface of hyperelastic myocardium. As evident from Figs. 8 and 9, the temperature distribution attained after 60 s of cardiac ablation is higher in the case for which the tissue deformation was neglected. This prevailing difference can be attributed to the fact that under the same insertion depth of the electrode within the cardiac tissue, neglecting tissue deformation results in a higher percentage of contact between the electrode and the tissue, and thus subsequently higher energy delivery as compared to the case where tissue deformation was considered. The differences in the ablation volume obtained for different values of electrode insertion taking into account and neglecting tissue deformation have been presented in Fig. 10. As evident from Fig. 10, the differences in the obtained ablation volumes after 60 s of cardiac ablation are quite negligible up to electrode insertion depth of 1.5 mm, and then increases significantly. In particular, for the electrode insertion depth of 2 mm, the increase in ablation volume obtained with neglecting tissue deformation has been found to be 19.95% and 24.23% in comparison to the ablation volume predicted with considering the tissue deformation at the electrode-tissue interface for the higher and lower blood flow rates, respectively. Thus, the predicted results of the present numerical study suggest that tissue deformation could play a vital role in accurately quantifying the treatment outcomes of the cardiac ablation.

The von Mises stresses arising from the thermal exposure of the cardiac tissue to elevated temperature during the RFA procedure have been presented in Fig. 11. It is noteworthy to mention that in continuum mechanics, the von Mises stress is the criterion for calculating whether the induced stress will cause the failure of the material or not. As earlier, the left side of Fig. 11 is with high

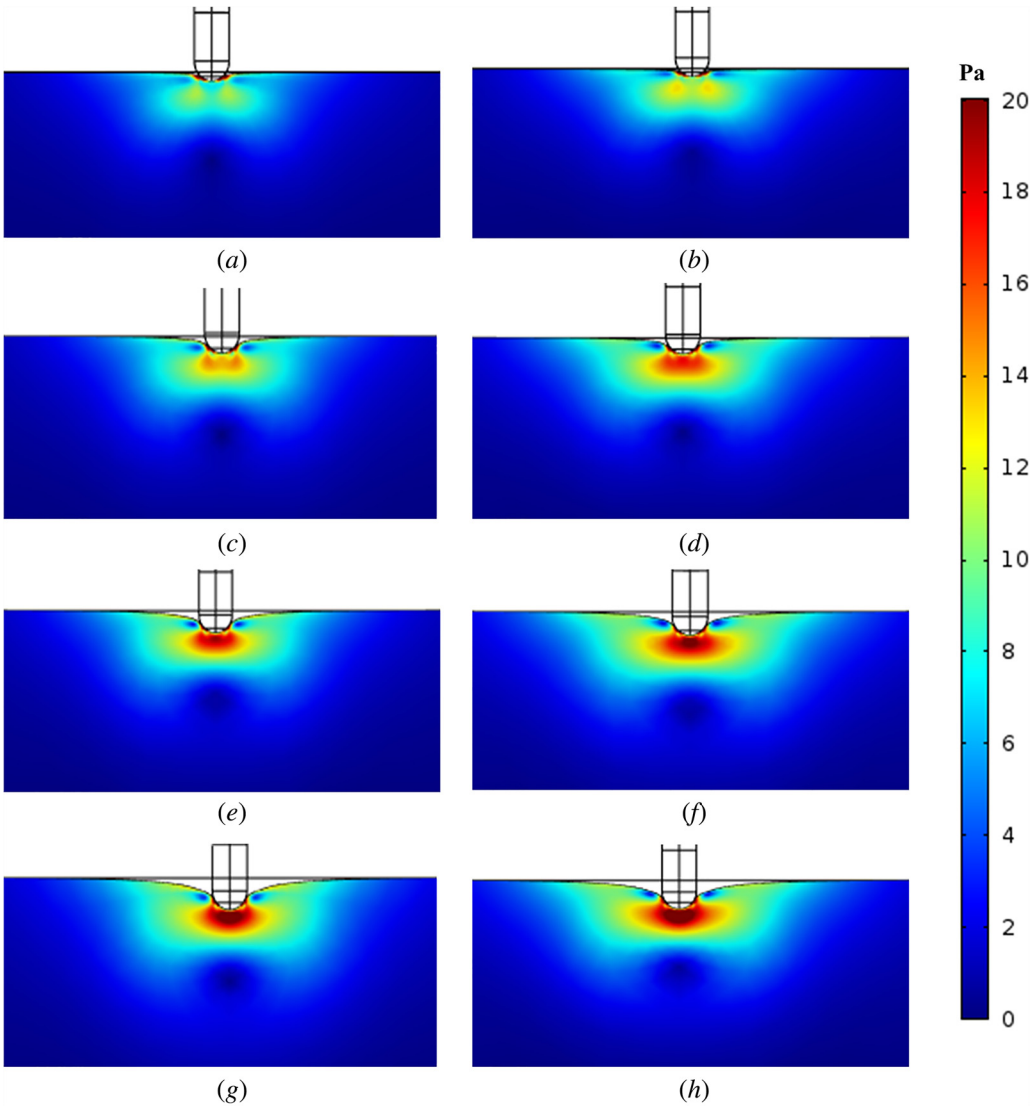

Fig. 11 Von Mises stress distributions within the tissue after 60 s of cardiac ablation under the electrode insertion depth of: (*a*) and (*b*) 0.5 mm, (*c*) and (*d*) 1 mm, (*e*) and (*f*) 1.5 mm, and (*g*) and (*h*) 2 mm. (*a*), (*c*), (*e*), and (*g*) are for high blood flow while (*b*), (*d*), (*f*), and (*h*) are under low blood flow conditions inside the cardiac chamber.

blood flow condition while the right side is with low blood flow condition. Further, Figs. 11(*a*) and 11(*b*) is for 0.5 mm insertion depth, Figs. 11(*c*) and 11(*d*) is for 1 mm insertion depth, Figs. 11(*e*) and 11(*f*) is for 1.5 mm insertion depth, and Figs. 11(*g*) and 11(*h*) is for 2 mm insertion depth. As evident from Fig. 11, the maximum value of the von Mises stress induced within the cardiac tissue has been found to be concentrated close to the vicinity of the electrode tip where the high temperature is found. The maximum value of the von Mises stress induced due to thermal heating of cardiac tissue during RFA lies in the range of 0–101 Pa. Further, the induced von Mises stress at the end of 60 s of RFA procedure for low blood flow is slightly higher in comparison to that of high blood flow condition. This can be attributed to the higher value of maximum temperature obtained in the case of low blood flow compared to the high blood flow condition. Thus, the proposed model of cardiac ablation utilizing a coupled electrothermomechanical framework would be useful in providing a better and more accurate a priori estimates of treatment outcomes to further enhance the effectiveness of the procedure. Overall, the results reported in this study in terms of both temperature distribution and ablation volume are consistent with the previously reported numerical studies that also accounted for the mechanical deformation induced at the electrode-tissue interface during cardiac ablation [18,19]. Importantly, the cardiac tissue has been modeled as an elastic material in Ref. [18] and hyperelastic material in Ref. [19]. Extending this notion of the mechanical deformation induced due to electrode insertion, we reported a fully coupled electrothermomechanical model to also account for the thermal stresses induced within the cardiac tissue during cardiac ablation. We found that the ablation volume during cardiac ablation increases with an increase of the insertion depth which is concurrent with the results reported in Refs. [18] and [19]. Future studies will be based on developing the fully coupled three-dimensional model whereby the blood flow inside the cardiac chamber and the saline flow through the holes of an open-irrigated electrode will be modeled utilizing the Navier–Stokes equations and the blood will be modeled as a non-Newtonian fluid. We also plan to incorporate the full thorax model as recently reported in Refs. [25] and [26].

Conclusions

We have reported a fully coupled electrothermomechanical model of cardiac ablation for a more accurate prediction of the treatment outcomes. Our findings suggest that the ablation volume attained during cardiac ablation is significantly dependent on the contact force at the electrode-tissue interface as well as the blood flow rate. We have also reported the thermal stress distributions induced due to the elevated temperature attained within the cardiac tissue during RFA.

Acknowledgment

This is an extended version of the paper (IMECE2020-23367) that has been accepted for publication and will be presented at the ASME's International Mechanical Engineering Congress and Exposition (IMECE2020) to be held at Portland, OR from November 13–19, 2020. Authors are grateful to the NSERC and the CRC Program for their support. RM is also acknowledging support of the BERC 2018-2021 program and Spanish Ministry of Science, Innovation and Universities through the Agencia Estatal de-Investigacion (AEI) BCAM Severo Ochoa excellence accreditation SEV-2017-0718 and the Basque Government fund AI in BCAM EXP. 2019/00432.

Nomenclature

c = specific heat capacity (J/(kg·K))
C = tissue water content
E = electric field intensity (V/m)
$\bar{E}$ = Young's modulus of elasticity (Pa)
F = deformation gradient
$\bar{F}$ = exterior body force (N)
h = enthalpy (J/m^3)
H_{fg} = latent heat (J/m^3)
J = volume ratio
J^{th} = thermal volume ratio
k = thermal conductivity (W/m·K)
Q_m = metabolic heat generation (W/m^3)
r, z = position/coordinates (m)
t = time (s)
T = temperature (K)
T_b = core blood (or baseline) temperature (= 37 °C)
u = mechanical displacement vector (m)
V = electric potential (V)
$\dot{V}$ = ablation volume (mm^3)
W = strain energy (J/m^3)

Greek Symbols

α = thermal expansion coefficient (K^{-1})
δ = Kronecker delta function
ε = mechanical strain
ε^{th} = thermal expansion strain
ν = Poisson's ratio
ρ = density (kg/m^3)
σ = electrical conductivity (S/m)
$\bar{\sigma}$ = mechanical stress (Pa)
ω_b = blood perfusion rate (s^{-1})

Subscripts

b = blood
g = gas phase
l = liquid phase
0 = Initial value at baseline temperature

References

[1] Almekkawy, M., Chen, J., Ellis, M. D., Haemmerich, D., Holmes, D. R., Linte, C. A., Panescu, D., Pearce, J., Prakash, P., and Zderic, V., 2020, "Therapeutic Systems and Technologies: State-of-the-Art Applications, Opportunities, and Challenges," IEEE Rev. Biomed. Eng., **13**, pp. 325–339.
[2] Kok, H. P., Cressman, E. N., Ceelen, W., Brace, C. L., Ivkov, R., Grüll, H., Ter Haar, G., Wust, P., and Crezee, J., 2020, "Heating Technology for Malignant Tumors: A Review," Int. J. Hyperthermia, **37**(1), pp. 711–741.
[3] Singh, S., and Melnik, R., 2020, "Thermal Ablation of Biological Tissues in Disease Treatment: A Review of Computational Models and Future Directions," Electromagn. Biol. Med., **39**(2), pp. 49–88.
[4] Zhang, B., Moser, M. A., Zhang, E. M., Luo, Y., Liu, C., and Zhang, W., 2016, "A Review of Radiofrequency Ablation: Large Target Tissue Necrosis and Mathematical Modelling," Phys. Med., **32**(8), pp. 961–971.
[5] Huang, S. K. S., and Miller, J. M., 2020, *Catheter Ablation of Cardiac Arrhythmias*, Elsevier, Philadelphia, PA.
[6] Linte, C. A., Camp, J. J., Rettmann, M. E., Haemmerich, D., Aktas, M. K., Huang, D. T., Packer, D. L., and Holmes, D. R., 2018, "Lesion Modeling, Characterization, and Visualization for Image-Guided Cardiac Ablation Therapy Monitoring," J. Med. Imaging, **5**(02), p. 1.
[7] Singh, S., and Melnik, R., 2019, "Coupled Thermo-Electro-Mechanical Models for Thermal Ablation of Biological Tissues and Heat Relaxation Time Effects," Phys. Med. Biol., **64**(24), p. 245008.
[8] Singh, S., and Repaka, R., 2018, "Quantification of Thermal Injury to the Healthy Tissue Due to Imperfect Electrode Placements During Radiofrequency Ablation of Breast Tumor," J. Eng. Sci. Med. Diagn. Ther., **1**(1), p. 011002.
[9] Fang, Z., Zhang, B., Moser, M., Zhang, E., and Zhang, W., 2018, "Design of a Novel Electrode of Radiofrequency Ablation for Large Tumors: A Finite Element Study," J. Eng. Sci. Med. Diagn. Ther., **1**(1), p. 011001.
[10] Singh, S., and Repaka, R., 2018, "Numerical Study to Establish Relationship Between Coagulation Volume and Target Tip Temperature During Temperature-Controlled Radiofrequency Ablation," Electromagn. Biol. Med., **37**(1), pp. 13–22.
[11] Singh, S., and Repaka, R., 2017, "Temperature-Controlled Radiofrequency Ablation of Different Tissues Using Two-Compartment Models," Int. J. Hyperthermia, **33**(2), pp. 122–134.
[12] Singh, S., and Repaka, R., 2017, "Effect of Different Breast Density Compositions on Thermal Damage of Breast Tumor During Radiofrequency Ablation," Appl. Therm. Eng., **125**, pp. 443–451.
[13] Zhang, B., Moser, M. A., Zhang, E. M., Luo, Y., Zhang, H., and Zhang, W., 2014, "Study of the Relationship Between the Target Tissue Necrosis Volume

and the Target Tissue Size in Liver Tumours Using Two-Compartment Finite Element RFA Modelling," Int. J. Hyperthermia, **30**(8), pp. 593–602.
[14] Gonzalez-Suarez, A., and Berjano, E., 2016, "Comparative Analysis of Different Methods of Modeling the Thermal Effect of Circulating Blood Flow During RF Cardiac Ablation," IEEE Trans. Biomed. Eng., **63**(2), pp. 250–259.
[15] González-Suárez, A., Berjano, E., Guerra, J. M., and Gerardo-Giorda, L., 2016, "Computational Modeling of Open-Irrigated Electrodes for Radiofrequency Cardiac Ablation Including Blood Motion-Saline Flow Interaction," PLoS One, **11**(3), p. e0150356.
[16] Pérez, J. J., González-Suárez, A., and Berjano, E., 2018, "Numerical Analysis of Thermal Impact of Intramyocardial Capillary Blood Flow During Radiofrequency Cardiac Ablation," Int. J. Hyperthermia, **34**(3), pp. 243–249.
[17] González-Suárez, A., Pérez, J. J., and Berjano, E., 2018, "Should Fluid Dynamics Be Included in Computer Models of RF Cardiac Ablation by Irrigated-Tip Electrodes?," Biomed. Eng. Online, **17**(1), p. 43.
[18] Petras, A., Leoni, M., Guerra, J. M., Jansson, J., and Gerardo-Giorda, L., 2019, "A Computational Model of Open-Irrigated Radiofrequency Catheter Ablation Accounting for Mechanical Properties of the Cardiac Tissue," Int. J. Numer. Methods Biomed. Eng., **35**(11), p. e3232.
[19] Yan, S., Gu, K., Wu, X., and Wang, W., 2020, "Computer Simulation Study on the Effect of Electrode–Tissue Contact Force on Thermal Lesion Size in Cardiac Radiofrequency Ablation," Int. J. Hyperthermia, **37**(1), pp. 37–48.
[20] Singh, S., Repaka, R., and Al-Jumaily, A., 2019, "Sensitivity Analysis of Critical Parameters Affecting the Efficacy of Microwave Ablation Using Taguchi Method," Int. J. RF Microwave Comput.-Aided Eng., **29**(4), p. e21581.
[21] Singh, S., and Melnik, R., 2020, "Domain Heterogeneity in Radiofrequency Therapies for Pain Relief: A Computational Study With Coupled Models," Bioengineering, **7**(2), p. 35.
[22] Holzapfel, G. A., Gasser, T. C., and Ogden, R. W., 2000, "A New Constitutive Framework for Arterial Wall Mechanics and a Comparative Study of Material Models," J. Elast. Phys. Sci. Solids, **61**, pp. 1–48.
[23] COMSOL Multiphysics, 2019, "COMSOL Multiphysics: Structural Mechanics Module User's Guide (Version: 5.5)," COMSOL Multiphysics, accessed Sept. 9, 2020, https://doc.comsol.com/5.5/doc/com.comsol.help.sme/StructuralMechanicsModuleUsersGuide.pdf
[24] COMSOL, 2019, "COMSOL Multiphysics® v. 5.5," COMSOL AB, Stockholm, Sweden, accessed Sept. 9, 2020, http://www.comsol.com
[25] Nguyen, D. M., Qian, P., Barry, T., and McEwan, A., 2020, "The Region-of-Interest Based Measurement Selection Process for Electrical Impedance Tomography in Radiofrequency Cardiac Ablation With Known Anatomical Information," Biomed. Signal Process. Control, **56**, p. 101706.
[26] Irastorza, R. M., Gonzalez-Suarez, A., Pérez, J. J., and Berjano, E., 2020, "Differences in Applied Electrical Power Between Full Thorax Models and Limited-Domain Models for RF Cardiac Ablation," Int. J. Hyperthermia, **37**(1), pp. 677–687.